www.acsnano.org

Chiroptical Control of Gold Nanoparticle **Growth through Combination of a Multimodal Chirality Inducer and Surfactant Counterion**

In Han Ha, [¶] Kyle Van Gordon, [¶] Robin Girod, [¶] Jeong Hyun Han, [¶] Evgenii Vlasov, Sandra Baúlde, Jesús Mosquera, Ki Tae Nam,* Sara Bals,* and Luis M. Liz-Marzán*



Downloaded via UNIV OF ANTWERPEN on August 28, 2025 at 10:42:37 (UTC). See https://pubs.acs.org/sharingguidelines for options on how to legitimately share published articles.

Cite This: ACS Nano 2025, 19, 28530-28539



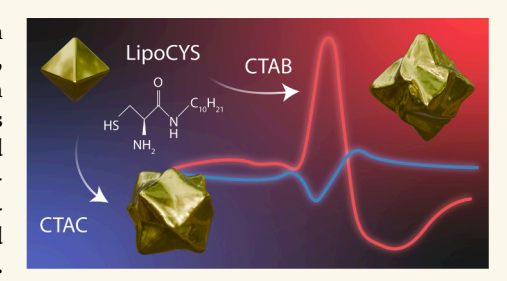
ACCESS I

Metrics & More

Article Recommendations

Supporting Information

ABSTRACT: Chiral plasmonic nanomaterials display strong interactions with circularly polarized light, offering significant potential in chirality sensing, enantioselective catalysis, and biomedical applications. While recent advances in seeded-growth synthesis have yielded complex chiral gold nanostructures through chemically induced or micelle-directed growth mechanisms, detailed intercorrelated mechanisms remain elusive. In this context, we have systematically investigated the versatility of the chiral inducer 2-amino-N-decyl-3mercaptopropanamide (LipoCYS), which incorporates both an amino acid moiety and an aliphatic chain designed to bridge both established mechanisms. By employing cubic and octahedral achiral gold seeds and varying the surfactant



halides, along with the concentration of LipoCYS, we generated a wide range of chiral morphologies, from twisted helicoids to intricate wrinkled spheres and intermediate structures. Advanced electron microscopy, including electron tomography, enabled comprehensive three-dimensional characterization and revealed distinct chiral morphological transitions and their correlations with chiroptical properties. Excellent agreement was found with the simulation results, thereby validating the representativeness of the microscopic analysis. Our findings expand the synthetic toolbox available for the precise control of nanoparticle chirality, providing deeper insights into the mechanisms of chiral growth and enhancing their potential for tailored applications.

KEYWORDS: chirality, plasmonics, circular dichroism, chiral nanoparticles, growth mechanism

INTRODUCTION

The introduction of chiral molecules during the seeded growth of colloidal plasmonic nanoparticles (NPs) has marked a milestone in an apparently mature field, granting access to a wide library of complex morphologies with reduced symmetry. Along with morphological chirality, these materials display rich optical activity, related to chiral surface plasmon resonance modes that may couple with each other along the entire nanoparticle surface.¹⁻³ Although multiple variations of chiral seeded growth have been reported, mechanistic aspects are still under intense debate. The general principles applying to the synthesis of achiral nanoparticles are also of relevance here: symmetry breaking via a stepwise growth approach and the use of surfactants, among other additives, favor anisotropic/ dissymmetric growth.^{4,5} Although some examples are known of chiral growth for other metals, this process has been mostly demonstrated in the synthesis of gold nanoparticles. A common feature in all reported syntheses is the reduction of gold ions on achiral gold seeds in the presence of a chiral inducer that guides seeded growth into a chiral morphology.

The concentrations of the chiral inducer, surfactant, gold ions, and achiral seeds, as well as the growth conditions including pH, temperature, and reaction time, greatly influence the process.

Two ground-breaking reports marked the progress in chiral nanoparticle synthesis, apparently based on different mechanisms directed by the chemical nature of the molecular chiral inducer. The most popular method can be termed "chemically induced" because it involves the use of thiolated chiral molecules that bind strongly onto gold surfaces and influence asymmetric growth on high-index planes of the growing nanoparticles.8 This method has been applied to achiral gold seeds with various shapes (cubes, octahedra, rhombic

Received: May 9, 2025 Revised: July 19, 2025 Accepted: July 21, 2025 Published: August 1, 2025





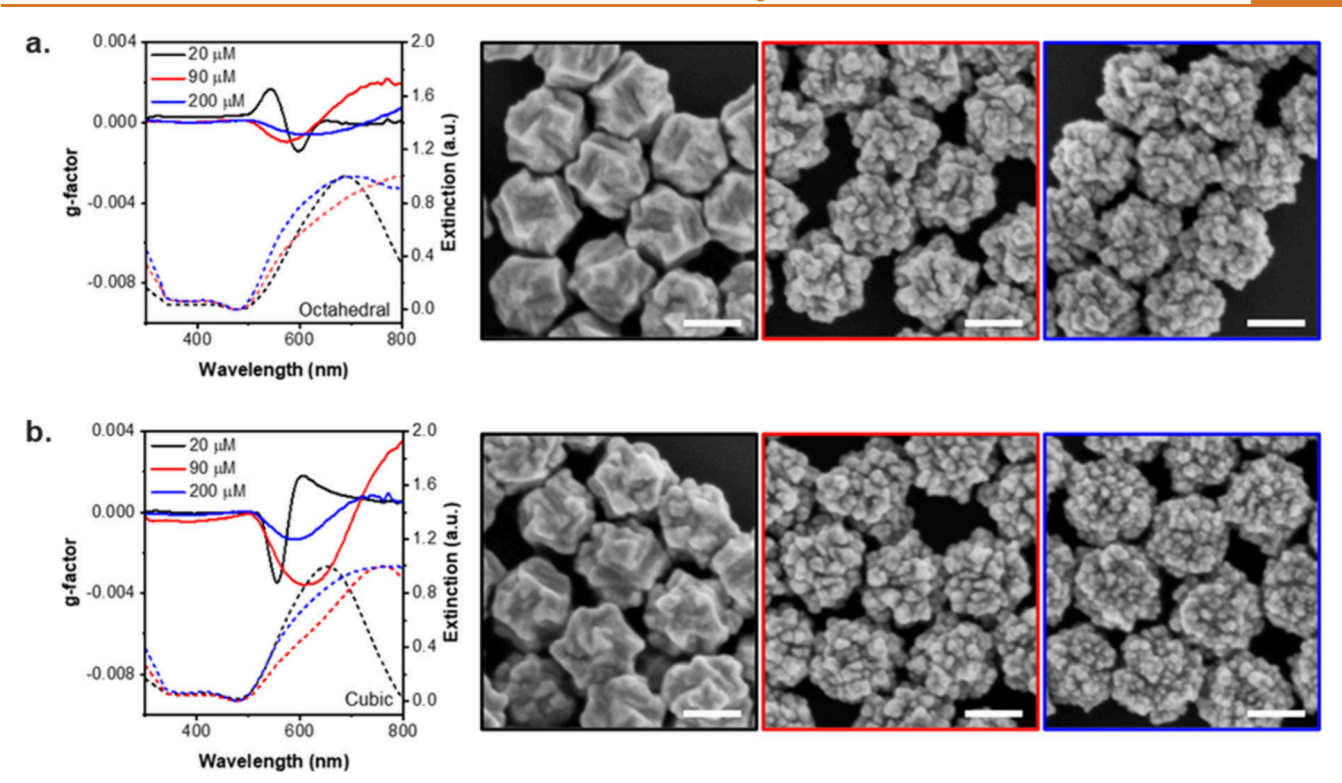


Figure 1. Chiroptical g-factor (solid lines), extinction (dashed lines) spectra, and SEM images of chiral nanoparticles synthesized using octahedral (a) and cubic (b) Au NPs as seeds, with varying concentrations of (R)-LipoCYS. Image frames are color-coded according to the legend in the plots. All scale bars represent 100 nm.

dodecahedra, nanorods) using mainly amino acids—cysteine (CYS), glutathione (GSH), etc.—as chiral inducers, together with the surfactant cetyltrimethylammonium bromide (CTAB), and leading to high optical activity in the visible range. A second growth mechanism (micelle-directed) proposes the formation of helical micelles when a chiral cosurfactant, such as 1,1-binaphthyl-2,2-diamine (BIN-AMINE) is mixed with cetyltrimethylammonium chloride (CTAC). Such worm-like micelles are hypothesized to dynamically adsorb on the surface of elongated gold nanoparticles (nanorods) and serve as a template for the (seeded) growth of quasihelical wrinkles on achiral gold nanorods.

The two distinct mechanisms of chiral growth identified so far provide a strong foundation for understanding the formation of uniform chiral gold nanostructures, marking a solid starting point in unveiling new scientific principles. However, additional or intercorrelated mechanisms may yet emerge, offering deeper insights into the evolution of chirality from an achiral state, a process that remains inherently complex with far-reaching implications. The recently reported phenomena of chiral inversion determined by the crystallinity of the starting seeds, ¹⁶ the expansion into alternative synthesis methods, ^{10,17} the emergence of new symmetry groups in chiral structures, ^{11,18} the utilization of novel chiral inducers, ¹⁹ and the expansion of the material library to other metal elements are examples of how these two mechanisms serve as inspiration for further developments.

With the aim to further understand chiral growth, the chiral molecule 2-amino-N-decyl-3-mercaptopropanamide (LipoCYS) has been reported to bridge the two previously proposed chiral growth mechanisms. ¹⁹ LipoCYS comprises a cysteine headgroup that may influence the growth of chiral facets (chemically induced mechanism), conjugated to an

aliphatic chain that provides a certain amphiphilic character and might form a micellar template with CTAC (micelle-directed mechanism). Using gold nanorods as achiral seeds, it was demonstrated that either twisted or wrinkled nanoparticles could be obtained via variation of the LipoCYS concentration: a low LipoCYS concentration yields twisted nanorods (alike the chemically induced growth mechanism), whereas at a high LipoCYS concentration, wrinkled nanorods (such as those derived from the micelle-directed growth mechanism) were obtained. LipoCYS is thus considered as a helpful tool for studying the potential combined application of the two established chiral growth mechanisms toward a broader synthetic toolbox of chiral nanoparticle morphologies.

A major question remains whether LipoCYS might also be applied to modulate chiral growth on more isotropic nanoparticle seeds, such as cubes or octahedra, which have been largely used within the chemically induced mechanism. We hypothesized that this strategy could lead to previously nonexisting, intricate morphologies, with complex chiroptical response related to light confinement at different regions of their three-dimensional (3D) nanoscale morphology. The analysis of the obtained chiral morphologies and corresponding shape-optical activity relationships requires access to their 3D geometries with high resolution. 20 Although conventional scanning electron microscopy (SEM) often provides images with rich morphological information, it lacks the spatial resolution needed to resolve nm-scale features in 3D. As a result, simulations of chiral plasmonic nanostructures typically rely on idealized models that may not fully capture the fine features of the nanoparticles and their evolution within the synthetic space.^{21–23} In this context, methods benefiting from the higher spatial resolution of scanning transmission electron microscopes (STEM) are gaining traction.²⁴ Especially for

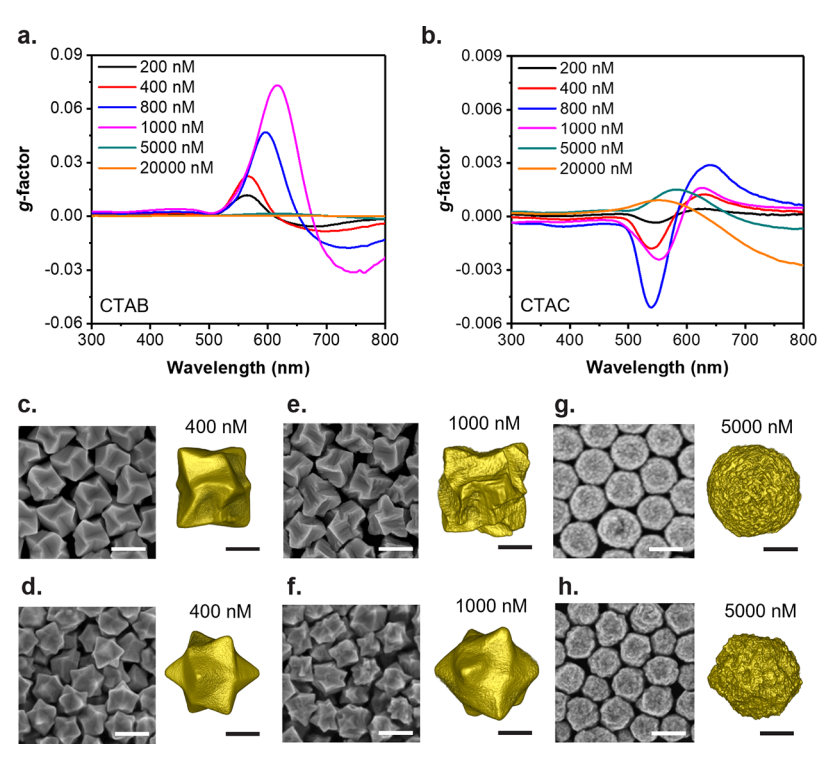


Figure 2. Chiroptical (g-factor) spectra and electron microscopy characterization of chiral products obtained using octahedral achiral Au NPs as seeds, and CTAB (a,c,e,g) or CTAC (b,d,f,h) as the surfactant in the synthesis, with 400 nM (c,d), 1000 nM (e,f), or 5000 nM (g,h) of (R)-LipoCYS. Images include SEM micrographs (left) and surface renderings from electron tomography reconstructions (right). Scale bars for SEM images are 200 nm and 100 nm for surface renderings.

nanoparticles without mirror symmetry, electron tomography is an important technique. Hereby, STEM projections measured at different angles serve as inputs for algorithms to compute a faithful 3D reconstruction of the specimen. Hore recently, secondary electron e-beam induced current (SEEBIC) imaging was demonstrated to be of use to obtain images with surface contrast at STEM resolution. By direct incorporation of real, more precise geometric information into electromagnetic numerical simulations, the complex chiral geometries of nanoparticles can be precisely correlated with their chiroptical characteristics in both near- and far-field regimes.

In the present work, we investigated the influence of the seed morphology (cubic or octahedral seeds) for different concentrations of tailored chiral inducer (R-LipoCYS) as well as the role of CTAB versus CTAC as the surfactants used in the micelle-directed and chemically induced strategies, respectively. We identify the effects of varying these synthetic parameters on the resulting morphologies and their plasmonic properties, highlighting those cases that require nanoscale analysis to link morphology with chiroptical behavior. In such cases, 3D electron microscopy characterization and electromagnetic simulations are leveraged to gain insights into the optical-structural relationships and the underlying chiral growth mechanisms. This systematic approach provides an enhanced comprehension of the available synthetic toolbox and offers novel insights into the mechanisms driving chirality in these systems.

RESULTS AND DISCUSSION

Our first set of experiments explored the variable of starting seed morphology in chiral growth, which has proven to be a highly influential factor for the chiroptical signature of the products.¹⁶ Cubic and octahedral achiral gold nanoparticles were used as seeds for chiral reactions involving similar chemical parameters and LipoCYS concentrations (20, 90, and 200 µM) as previously reported for nanorods (see Nanoparticle Synthesis).¹⁹ We observed concentration-dependent optical and structural evolutions of the chiral products for both achiral seed morphologies (Figure 1). Although the magnitude of the chiroptical signal was significantly decreased, the overall spectral broadening trend was similar compared to those obtained using achiral gold nanorods as seeds. 19 SEM images confirmed that this optical variation correlates with a morphological evolution from smooth to wrinkled particles, resembling the morphological transition previously described for nanorods. However, for the lower LipoCYS concentration (20 μ M), the sign of the g-factor is opposite for the chiral particles synthesized from cubes or octahedra, even though both seeds were of comparable dimensions, 26,27 and chiral growth was carried out under identical conditions. These results suggest that the achiral seed geometry is more relevant at low LipoCYS concentrations, where the chemically induced chiral growth mechanism is expected to be most relevant. This inference is consistent with previous reports by Nam and coworkers, 27,28 where helicoids were obtained using the same cysteine enantiomer but differing starting seeds: cubes became stellated octahedrons (termed Helicoid I), whereas cuboctahedrons became rhombic dodecahedrons (termed Helicoid IV), with inverted chiroptical signatures.

After confirming the ability of LipoCYS to induce chiral growth, we studied the effect of surfactant counterion (CTAC vs CTAB), using octahedral achiral gold nanoparticles as seeds and similar chemical parameters as previously reported to yield helicoids (see Nanoparticle Synthesis). With both CTAC and CTAB surfactant, the use of LipoCYS as a chiral inducer

enabled the synthesis of products with chiroptical signal in the size range of 180 to 220 nm (Figures 2 and S1). This comes in contrast to previous reports in which CTAC was seen to hinder chemically induced chiral growth due to the low binding affinity of chloride ions to the Au surface.²⁹ Notwithstanding, significant differences are observed in the corresponding chiroptical spectra for a range of LipoCYS concentrations (Figure 2a,b). Under CTAB conditions, increasing the LipoCYS concentration up to 1000 nM resulted in a gradual redshift of the g-factor spectrum, reaching a maximum absolute g-factor of approximately 0.08 at around 600 nm. At even higher LipoCYS concentrations, a sharp decrease in the chiroptical response was observed. In contrast, CTAC yielded an order of magnitude lower intensity, exhibiting a maximum absolute g-factor of 0.005 at around 550 nm when the LipoCYS concentration reached 800 nM. Further increase in LipoCYS concentration led to a pronounced redshift of the g-factor spectrum, maintaining a major negative component. Most remarkably, the sign of the circular dichroism (CD) signal was reversed when CTAC was used instead of CTAB.

A first analysis of the morphological evolution was carried out by SEM imaging and electron tomography in high-angle annular dark field (HAADF)-STEM mode (Figures 2c-h and S2, Supplementary Videos 1 and 2). The obtained images and 3D reconstructions show that, under both surfactant conditions and up to a LipoCYS concentration of 1000 nM, helicoid-like structures resembling those conventionally formed via chemically induced growth mechanisms were produced (Figures 2c-f and S2a,b). Accordingly, a 432 geometry is evidenced by the 3D reconstructions: two types of vertices with 4-fold and 3-fold rotational symmetry can be identified, along with grooves showing 2-fold rotational symmetry (Figure S3). The vertices are linked by ridges so that when viewed along a 4-fold symmetry axis ($\langle 100 \rangle$ zone axis), the particles show a left-handed "pinwheel" geometry, whereas a right-handed geometry is observed when the particles are viewed along their 3-fold symmetry axis (\langle 111) zone axis). Importantly, particles grown in the presence of CTAB featured more prominent 4-fold vertices, whereas those grown in the presence of CTAC featured more prominent 3fold vertices (Figure S3). This discrepancy will be further discussed below.

At higher LipoCYS concentrations (≥5000 nM), SEM and electron tomography results revealed dramatic structural changes. Regardless of the choice of halide, smooth and twisted facets disappeared; instead, quasispherical morphologies with complex surface features and no evident faceting or geometry were produced (Figures 2g,h and S2c,d). To visualize these features at higher resolution, we performed surface imaging using SEEBIC in STEM mode (Figure S4) and characterized 4-10 particles for each sample. Representative images are shown in Figure S5a. The SEEBIC images confirmed the presence of thin wrinkles on these particles, thereby supporting the prevalence of a templating effect in a micelle-directed growth mechanism at high LipoCYS concentrations. However, differences were observed between such wrinkled particles. Specifically, the particles grown in CTAC and 5000 nM [LipoCYS] featured relatively smaller wrinkles and groove (interwrinkle) width than other samples (Figure S5b). Those grown in CTAB and 20000 nM [LipoCYS] had less defined features, as shown by a significantly smaller groove length (Figure S5c), in correlation with their lower chiroptical signal. Samples grown in 5000 nM [LipoCYS] in CTAB and 20000 nM [LipoCYS] in CTAC displayed qualitatively and quantitatively similar morphologies. These observations suggest a different micellar behavior depending on the concentration and halide choice.

We also observed evidence that at intermediate LipoCYS concentrations mixed modalities of chirality transfer may exist. Notably, the 432 particles grown in CTAB and with 800 and 1000 nM [LipoCYS] displayed secondary striated features following the twisted surfaces, similar to those formed under a micelle-directed growth mechanism (Figures 2e and S2b). In contrast to a previous report describing chemically induced chiral morphologies with surface roughness produced under an active growth mechanism,³⁰ the secondary features we observe appear to follow the underlying helical surface more closely, with fine grooves similar to those formed under a micelledirected growth mechanism. In addition, a hexagonal crosssection and poorly defined protruding tips are observed in the SEM, electron tomography, and SEEBIC images of the wrinkled particles grown in CTAC with 5000 nM [LipoCYS] (Figures 2h and S5a), which was confirmed by an overall lower circularity of these particles compared to other wrinkled products (Figure S5e). This effect may also be due to a dual LipoCYS action whereby the initial seed would evolve into a different faceted intermediate, as previously reported for Au nanorod seeds, prior to wrinkle growth.19

Overall, these results suggest that LipoCYS retains its dual modality of chirality transfer, acting through chemisorption and chiral facet stabilization at low concentration via a dominating micelle-templating effect at higher concentration and possibly with a combination of effects at intermediate concentrations. It is also clear that, in the presence of LipoCYS, chiral growth can be achieved using either CTAB or CTAC. The results bear significant differences, which we hypothesize relate to the different adsorption energies of halides (e.g., Br⁻, Cl⁻ ions) on high-index facets during chiral growth. It has also been reported that the CTA⁺ chain and halide ions from CTAB (or CTAC) may have a cooperative effect during anisotropic growth, via passivation and etching of high-index crystal facets.

We then investigated whether a detailed morphological analysis of the products with 432 geometry could provide insights into the observed chiroptical trends. As noted above, it is clear that particles grown in CTAB showed more prominent 4-fold vertices than those grown in CTAC, which was quantitatively confirmed by measurements of the helical branch length from tomography reconstructions (Figure S6). Furthermore, increasing g-factors were found to correlate with this increase in prominence. This is, for instance, visible in a plot of the ratio of the length of 4-fold branches to 3-fold branches against the g-factor of the sample (Figure 3a,b). The effect of the finer features appearing in CTAB at intermediate LipoCYS concentrations is uncertain, but we postulate that their alignment with the underlying chiral facets creates secondary chiral features that reinforce the overall optical activity. Furthermore, we quantitatively assessed the asymmetry of the reconstructed particles by measuring the difference between a particle and its optimally aligned mirror image (Figures 3c and S7). Our asymmetry measure is conceptually related to the well-established Hausdorff chirality measure 35,36 but is rendered computationally tractable on full-scale tomography reconstructions by replacing the Hausdorff distance with calculation of the nonoverlapping fraction

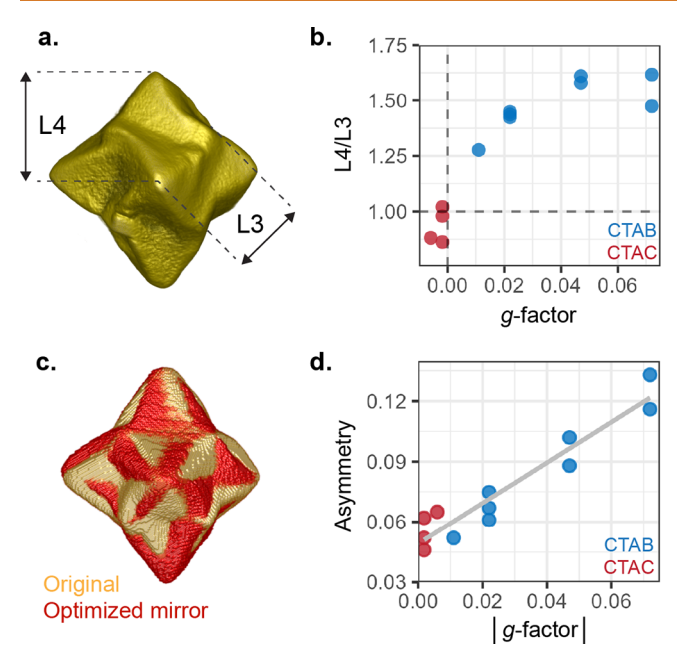


Figure 3. Optical-structural relationships in 432 LipoCYS helicoids. (a) Branch length measurements exemplified on an electron tomography reconstruction from a particle grown in the presence of CTAB and 400 nM LipoCYS. (b) Dependence of the peak g-factor on the branch prominence measured as the L4/L3 ratio measured in particles grown in CTAC or CTAB and different LipoCYS concentrations. (c) Result from alignment optimization between the particle in (a) and its mirror image to enable the calculation of asymmetry. (d) Dependence of the absolute value of the peak g-factor on particle asymmetry, measured as the nonoverlapping volume fraction between a particle and its mirror image. The gray line shows the linear regression model.

between two volumes (Characterization).²⁴ Overall, particles grown in CTAB displayed a higher asymmetry measure than those grown in CTAC (Figure 3d), in relation to their sharper and more prominent facets. Across all particles with a clear 432 geometry, the asymmetry measure was found to correlate linearly with higher g-factors (Figure 3d). These results suggest that more prominent helical vertices with a higher degree of geometrical asymmetry, possibly in relationship to secondary surface features, reinforce the optical asymmetry.

Finally, we investigated the CD sign inversion between 432 particles grown in CTAC and CTAB. From the tomography reconstructions, we find a clear correlation between this sign and the prominence of 4-fold vertices vs 3-fold vertices (Figure 3b). Given that these features are of opposite geometrical handedness, we hypothesize that those dominating the morphology will also dominate the overall optical handedness. We further tested this hypothesis through electromagnetic numerical simulations on the morphologies extracted from tomographic reconstructions, for a more accurate representation of the real samples. Specifically, reconstructions of particles grown in the presence of CTAC or CTAB at 400 nM [LipoCYS] were compared because their clean faceting allows us to isolate the effect of handedness reversal from those of other structural features seen at higher concentrations. The calculations were performed using COMSOL Multiphysics, a commercial Maxwell's equations solver based on the finite element method (FEM).²³ Upon import of 3D morphological data, their absorption and scattering cross-section spectra were calculated for illumination with left- and right-handed

circularly polarized (LCP and RCP) plane wave incidence (handedness defined from the perspective of the detector, i.e. IUPAC convention). The differential extinction cross-section, which corresponds to the macroscopic circular dichroism, was calculated as the difference of the sum of absorption and scattering cross-sections for LCP and RCP. 37 A total number of 26 incidence directions were considered: 6×4 -fold, 8×3 -fold, and 12×2 -fold symmetries under the 432 symmetry, to represent all possible directions for particles under Brownian motion (Figure 4a). 38,39 Since there is no difference in

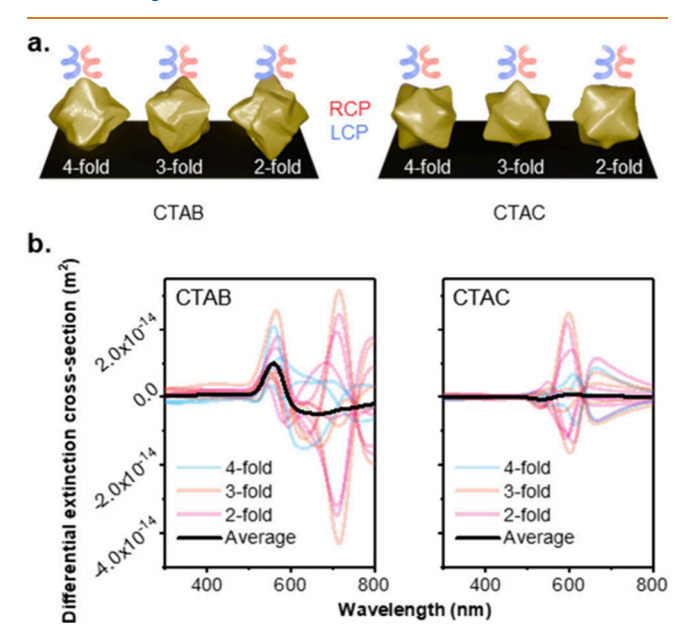


Figure 4. (a) Simulation geometry and (b) differential extinction cross-section spectra of particles synthesized with (a,b) (left) CTAB and (a,b) (right) CTAC, at 400 nM [LipoCYS]. Particles were illuminated from 26 different incident directions along their 4-, 3-, and 2-fold axes, considering a 432 symmetry. The thinner lines represent the spectra for individual incidence directions, whereas the thicker black lines indicate their arithmetic average.

chiroptical responses for forward and backward incidence due to the Lorentz reciprocity theorem, even though 26 incident directions were considered, only spectra for half of them are depicted in Figure 4b. Also depicted in Figure 4b is the overall differential extinction cross-section spectrum (thick black line), which results from averaging over all 13 directions (thinner lines). The calculated average spectra for particles grown in CTAB and CTAC with 400 nM LipoCYS were found to be in good agreement with the experimentally measured spectra, showing the CD inversion around 550 nm and lower CD intensity for CTAC (c.f. Figure 2a,b). This agreement confirms that the random translational and rotational motions in solution are effectively accounted for by integrating across the selected incident directions. Examining the individual spectra, we interpret that the consistent sign of the differential extinction cross-section across most incident directions, indicating their uniform optical chirality, originates from the high symmetry of 432 of the particles. This trend is also quite evident in the respective contributions of absorption and scattering (Figure S8). The fluctuations in individual spectra at longer wavelengths appear to be predominantly governed by differences in the scattering. Further mode analysis based on multipole expansion indicates that the splitting of chiral

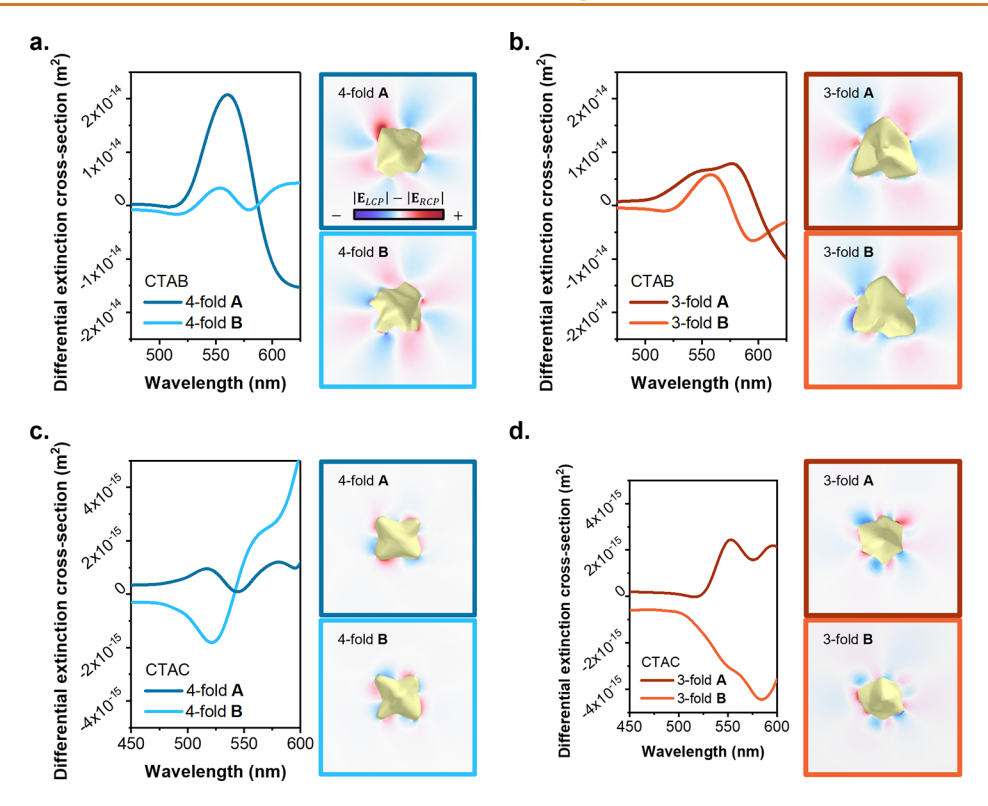


Figure 5. Numerically simulated differential extinction cross-section spectra and corresponding differential electric field distributions of particles synthesized with CTAB (a,b) and CTAC (c,d), depending on the illumination incidence direction. Panels (a,c) show results for 4-fold vertices, while panels (b,d) correspond to 3-fold vertices. Each panel shows the results for two arbitrarily selected directions, A and B, at the corresponding vertices. Image outlines are color-coded to match the legend of the plots.

eigenmodes arising from the interference between the electric dipole (ED) and magnetic dipole (MD) in that particular wavelength range is at the origin of plasmonic CD in these particles (Figure S9). As in previous reports, the simultaneous occurrence of ED and MD in chiral gold nanoparticles can be attributed to the influence of the current loop resulting from the morphological mirror symmetry breaking from 4/m3 2/m to 432 in the chirality evolution process. ^{40,41}

For completeness, we investigated the near-field response by calculating the electric field distribution around the particles for different incident directions of light. Figure 5 shows the differential extinction cross-section spectrum for incident directions facing 4-fold and 3-fold symmetry directions as well as the difference in the electric near-field intensity for LCP and RCP illumination at the wavelength corresponding to the maximum CD. Comparison of Figure 5a,b and Figure 5c,d shows that the particle synthesized using CTAB (Figure 5a,b), with a stronger chiroptical response, has an overall stronger field confinement compared to the particle synthesized with CTAC (Figure 5c,d). Comparing 4-fold (Figure 5a) and 3-fold (Figure 5b) directions, the dominating LCP/RCP components are opposite (i.e., for 4-fold, LCP (red) dominates, whereas for 3-fold, RCP (blue) dominates), following their geometric rotational directions. Even within the 4-fold direction (Figure 5a), slight differences in the morphological evolution led to subtle variations in the degree of field confinement, and the differential extinction cross-section is larger in the direction with stronger confinement. For the 3-fold direction (Figure 5b), although the RCP component is more pronounced at the near-field, the differential extinction cross-section spectrum has a positive value at that wavelength, suggesting that the far-field characteristics are more dominantly influenced by the overall

structure. The degree of morphological chirality expression is markedly lower in the particle synthesized with CTAC, which may underlie the inconsistency (direction-dependent sign reversals) observed in the chiroptical response to LCP and RCP light, as shown in Figure 5c,d.

CONCLUSIONS

We explored the synthesis space of the LipoCYS chiral inducer and helicoid protocols. It is found that on both cubic and octahedral seeds, LipoCYS induces chiral morphologies when used as a cosurfactant with either CTAB or CTAC. This highlights the versatility of LipoCYS beyond previously demonstrated nanorod systems and confirms that its dual functionality, involving chemically directed growth through chemisorption at low concentrations and micelle templating at high concentrations, can be applied to various seed geometries. Notably, chiral growth from octahedral seeds is achieved even in a CTAC environment, where chiral induction is typically suppressed, making LipoCYS a valuable platform for comparative studies. The range of generated morphologies was characterized using advanced TEM methods, tailored analytics, and optical simulations based on real threedimensional data to rationalize the observed structure-optical trends. In particular, we presented a measure of asymmetry based on the volumetric difference between a particle and its mirror image that is tractable on the scale of tomographic reconstructions and was shown to be strongly associated with the g-factor.

Our results disclose a parameter space based on the seed, the choice of halide, and the modality of chirality transfer within which chiroptical control can be achieved, in terms of both the sign of the circular dichroism and its magnitude. Importantly, tunability is demonstrated in homochiral conditions, i.e., with no need to change the handedness of the chiral inducer. Thus, this work broadens the chiral synthesis toolbox and provides insights into the mechanisms driving chirality in intricate nanocrystals.

MATERIALS AND METHODS

Chemicals. HAuCl₄·3H₂O (99.99% (metal basis)) was purchased from Alfa Aesar. Cetyltrimethylammonium bromide (CTAB; 99%), cetyltrimethylammonium chloride (CTAC; >98.0%) and CTAC solution (25 wt % in H₂O), potassium iodide (KI; 99.5%), sodium borohydride (NaBH₄; 99%), and ascorbic acid (AA; \geq 99%) were all purchased from Sigma-Aldrich. All reagents were used as received without further purification. Milli-Q water was used to prepare solutions. (*R*)-LipoCYS molecule was synthesized following a procedure reported in previous literature. ^{19,42}

Nanoparticle Synthesis. Synthesis of Octahedral and Cubic Seed Nanoparticles. Achiral single-crystal octahedral and cubic AuNPs were synthesized according to a stepwise protocol adapted from the literature. ^{26,43}

Preparation of CTAC-Stabilized Gold Nanoclusters (AuNCs). In a glass vial, 1.32 mL of 25% (w/v) CTAC was mixed with 250 μ L of a HAuCl₄ solution (0.01 M) and 8.43 mL of Milli-Q grade water; the solution was vortexed thoroughly. An ice-cold NaBH₄ solution (20 mM) was prepared, and 0.45 mL was quickly transferred to the above mixture, vortexing immediately for 2 min to quickly and completely reduce the gold salts. The solution was incubated at 25 °C for 1 h before use.

Preparation of Single-Crystal Octahedral Gold Nanoparticles (Octa-AuNPs). Gold octahedra were prepared according to established literature. Gold octahedra were prepared according to established literature. A 26.4 mL portion of 25% (w/v) CTAC was mixed with 5 mL of a HAuCl₄ solution (0.01 M) and 163 mL of Milli-Q grade water. After mixing gently by magnetic stirring, 4.4 mL of an ascorbic acid solution (40 mM) and 100 μ L of a KI solution (10 mM) were added with stirring to complete solution A. An aliquot of 995 μ L was taken from this solution, treated with 4 μ L of the solution containing CTAC-stabilized AuNCs, and immediately vortexed. Before the appearance of an intense pink color (~10 s), 900 μ L of the aliquot was transferred back to solution A, which was mixed via magnetic stirring for 30 s. The stirring was then stopped, and the solution was incubated at 30 °C for 15 min. Gold octahedra were isolated via two rounds of centrifugation (6708g, 15 min), redispersed in 3 mM CTAC, and evaluated by UV-vis spectroscopy (target LSPR peak position: 578 nm, with a tolerance of ± 2 nm).

Preparation of CTAB-Stabilized Gold Nanoclusters (AuNCs). In a glass vial, 7.5 mL of a CTAB solution (0.1 M) was mixed with 250 μL of a HAuCl $_4$ solution (0.01 M); the solution was vortexed thoroughly to combine. An ice-cold solution of NaBH $_4$ (10 mM) was prepared, and 0.8 mL was quickly transferred to the above mixture, vortexing immediately for 2 min to quickly and completely reduce the gold salts. The solution was aged at 25 °C for 1 h and diluted 1/10 into Milli-Q water before use.

Preparation of Single-Crystal Cubic Gold Nanoparticles (Cube-AuNPs). Gold cubes were prepared according to established literature. ^{26,43} 32 mL of a CTAB solution (0.2 M) was mixed with 4 mL of a HAuCl₄ solution (0.01 M) and gently stirred prior to addition (under stirring) of 19 mL of an ascorbic acid solution (0.4 M). The solution was further stirred for 30 s before addition of 100 μL of the solution of CTAB-stabilized AuNCs. The solution was stirred an additional minute and then incubated at 30 °C for 15 min. Gold cubes were isolated via two rounds of centrifugation (6708g, 15 min), resuspended in 1 mM CTAB, and evaluated by UV–vis spectroscopy (target LSPR peak position: 538 nm, with a tolerance of \pm 2 nm).

Seeded Chiral Growth in the Presence of LipoCYS: Protocol I. Chiral products were synthesized using achiral octahedral and cubic nanoparticles as seeds and in the presence of LipoCYS based on established literature. ¹⁹ Chiral growth was performed in 2 mL reaction volumes at 40 °C; CTAB and AA concentrations were kept constant

at 44 mM and 700 mM, respectively, and $[Au^{3+}]$: $[Au^0]$ was kept constant at 8.9 (185 μ M and 20.8 μ M, respectively). For all chiral preparations and after a 30 min incubation, chiral products were centrifuged (3000g, 10 min) and resuspended in Milli-Q water. This process was repeated twice to remove excess AA and CTAC from the solution.

Seeded Chiral Growth in the Presence of LipoCYS: Protocol II. The following describes an alternative protocol using LipoCYS and octahedral seeds for the production of helicoid-like particles. Chiral products were prepared in 5.35 mL reaction volumes at 30 °C; CTAC (or CTAB) and AA concentrations were kept constant at 14.9 and 8.8 mM, respectively, and $[\mathrm{Au}^{3+}]$: $[\mathrm{Au}^0]$ was kept constant at 40.8 (186 and 4.55 $\mu\mathrm{M}$, respectively). For all chiral preparations, and after a 2 h incubation, chiral products were spun down (4250g, 5 min) and resuspended in 1 mM CTAC (or CTAB). This process was repeated twice to remove excess AA and CTAC from solution.

Characterization. *Optical Measurements.* Circular dichroism (CD) and extinction spectra were obtained by using a J-1700 spectropolarimeter instrument (JASCO). Kuhn's dissymmetry factor (*g*-factor) was calculated from the measured CD values and extinction using

$$g\text{-factor} = 2\frac{A_L - A_R}{A_L + A_R} \propto \frac{\text{CD}}{\text{extinction}}$$
 (1)

Electron Microscopy. The synthesized products were characterized by using a scanning electron microscope (SIGMA, Zeiss). For electron tomography, particles were deposited on lacey carbon copper grids, 200 mesh, and the remaining ligands were cleaned using an established activated-charcoal method. 44 Acquisitions of tilt-series were done at a ThermoFisher Scientific Osiris or a Titan operated at 200 or 300 kV, respectively. Imaging was performed using high-angle annular dark field (HAADF) scanning transmission electron microscopy (STEM). Parameters were set to operate with a 50-60 pA probe current, 15-17 mrad convergence angle, and 46-215 mrad collection angle on the HAADF detector, equivalent to a 115 mm camera length on both microscopes. The sample holder was a Fischione 2020 single axis tomography holder, and the angular range typically spanned $[-75^{\circ}, +75^{\circ}]$. The acquisitions were done in "fast"tomography mode. 45 Movies were recorded during automated tilting using 2° angular increments and a 4-6 s pause at each acquisition angle, 0.8 μ s dwell time, and 1024² scan size resulting in 1 s per frame. Nondistorted images were isolated, and the resulting series were aligned with cross-correlation using a MATLAB code developed inhouse. Three-dimensional reconstructions were computed with the standard expected maximization (EM) algorithm using the ASTRA toolbox 2.1 for MATLAB. 46,47 Isosurface renderings were created using Amira (v5.4.0). For each sample analyzed, 2-5 reconstructions were obtained and compared with large-scale SEM images to identify the representative particles morphologies.

For secondary electron e-beam induced current (SEEBIC) imaging, we used a ThermoFisher Scientific Themis Z operated at 200 kV using a 250–500 pA probe current and a 17 mrad convergence angle. The principle of SEEBIC imaging is shown in Figure S4. SEEBIC measures a current arising from holes generated by the emission of SEs from the sample. The current flows to a current-sensing transimpedance amplifier (TIA), and the detected signal will be equal to but opposite the generated SE current. The detected signal can be mapped pixel-by-pixel to produce an image that is directly dependent on the SE yield for each probe position.

Prior to imaging, samples were Ar/O $_2$ plasma (3:1) cleaned to avoid a buildup of a layer of carbon contamination during the acquisition of SEEBIC data as well as to remove surface ligands hindering imaging. Images were acquired at 250–1000 μ s dwell time. A custom-made TIA with a total gain of 10 GV/A (0.4 GV/A at the first amplification stage) and bandwidth of 4 kHz, electrically connected to the sample via a DENS Solutions Wildfire holder, was used to convert the SEEBIC signal into a voltage signal digitized by the Attollight OUDS II scan engine, along with the amplified HAADF-STEM detector signal.

Morphological Analysis from Electron Tomography. The tomography reconstructions of particles with 432 geometries were quantitatively analyzed to measure the helical branch length and the asymmetry. For the branch length, representative electron tomography reconstructions were oriented to be along a <100> zone axis, i.e., with a 4-fold symmetry axis parallel to the viewing directions. Branch lengths were manually measured according to the schematic in Figure S6.

To quantify the asymmetry of the particles, we modified the Hausdorff chirality measure (HCM) approach for tractability with electron tomography data. (48,49) In HCM measurements, chirality is measured as the Hausdorff distance between a shape and its mirror image after having minimized the distance across translations and rotations of the mirror image. However, the Hausdorff distance is a computationally expensive measurement, especially on highly detailed voxelated tomography reconstructions. Here, we replaced the distance measurement with the disjunctive union of the volume and its mirror image. This effectively quantifies the overlap between 3D shapes and, after minimization, yields a measure of asymmetry that can be understood as the fraction of nonoverlapping volume between a shape and its mirror image.

For the calculations, a manual threshold was first placed to binarize the reconstructions, and the disjunctive union was calculated as

$$\Delta_{mirror}(V) = V \cup V' - V \cap V' \tag{2}$$

where Δ_{mirror} is the disjunctive union, V the binarized volume, and V' its mirror image (Figure S7). To obtain a measure of asymmetry a(V), the disjunctive union was minimized over all translations u, v, w and all rotations φ , θ , ω :

$$a(V) = \frac{\min_{\mathbf{u}, \mathbf{v}, \mathbf{w}, \boldsymbol{\varphi}, \boldsymbol{\theta}, \boldsymbol{\omega}} \boldsymbol{\Delta}_{mirror}(V)}{2V} \in [0, 1]$$
(3)

Prior to minimization, the center of mass of the binarized particles was calculated and centered within the volume. The volume was then downsized by local averaging so that the longest dimension was at most 150 voxels. The minimization was performed in two steps. First, a grid search was performed to find a global minima. The cost of this search scales with the number of translation and rotation steps following $n_{parameters}^{45}$ and with the number of voxels following $\sim n_{voxels}$. Thus, the grid search parameters were typically chosen to include 1–2 steps of translation in steps of 2 voxels, and 20–30 steps of rotation for each φ , θ , ω angles, with angular ranges covering 360° in all directions. This search was parallelized in Python and typically completed in 5–20 min. In a second step, the local minima was searched using the Nelder–Mead algorithm as implemented in SciPy, with the default parameters. The asymmetry code is available at https://github.com/robgirod/asymmetry-measure.

Morphological Analysis from SEEBIC Images. For the wrinkled products, measurements of the interwrinkle (groove) width and length, of the groove area coverage, and of the particle circularity were performed from the SEEBIC images using a custom MATLAB code. For each sample, 4–10 particles were analyzed. Each particle was first segmented from the HAADF-STEM images using Otsu thresholding. The circularity was directly assessed from connected component analysis using the built-in "regionprops" function. These binary masks were applied to SEEBIC images to isolate single particles for analysis. For groove measurements, the contrast within the SEEBIC images of each particle was first leveled using a rolling-ball background subtraction. The grooves were then segmented using an adaptive threshold. The width was obtained using a Euclidean distance transform, whereas the length was calculated from the topological skeleton.

Numerical Simulations. To calculate the far- and near-field plasmonic chiroptical response of chiral nanoparticles, a commercial finite element method (FEM)-based 3D Maxwell equation solver, COMSOL Multiphysics, was used. The simulation domain was designed as a spherical core—shell structure with a perfectly matched layer (PML) surrounding the computational region to absorb residual electromagnetic waves. The particle model was constructed by

manually thresholding an electron tomography reconstruction and extracting the corresponding triangular mesh using the built-in Amira function. The refractive index of the surrounding medium was set to 1.33, and the particle model was positioned in the center. The extinction cross-section was obtained as the sum of the absorption and scattering cross-sections. The absorption cross-section was calculated by integrating resistive losses throughout the particle's volume, while the scattering cross-section was derived from the surface integral of the scattered Poynting vector at the domain boundary. The average differential extinction cross-section was retrieved by taking the arithmetic average of extinction cross sections over all possible symmetry axis of 432 as incident directions, which can be written as

$$\Delta \sigma_{avg}^{ext} = \frac{1}{N_{tot}} \sum_{\alpha} \sum_{i=1}^{N_{\alpha}} \Delta \sigma_{\alpha,i}^{ext}$$
(4)

where $\alpha \in \{\text{4-fold, 3-fold, 2-fold}\}$, $N_{4\text{-fold}} = 6$, $N_{3\text{-fold}} = 8$, $N_{2\text{-fold}} = 12$, and $N_{total} = 26$ regarding the 432 symmetry. The multipole coefficients were retrieved by expanding the electromagnetic field into vector spherical harmonic wave functions under the illumination of a linearly polarized light.

ASSOCIATED CONTENT

Supporting Information

The Supporting Information is available free of charge at https://pubs.acs.org/doi/10.1021/acsnano.5c07744.

Materials and methods; SEM images and electron tomography reconstructions of chiral products at various viewing angles; schematic of the SEEBIC imaging concept; SEEBIC images of chiral wrinkled nanoparticles; quantitative analysis of the SEEBIC images; variation of the branch length across synthesis parameters; workflow for asymmetry measure on a 432 LipoCYS helicoid; differential absorption and scattering cross-section spectra of 432 LipoCYS helicoids; multipole expansion of total extinction of 432 LipoCYS helicoids (PDF)

Video S1 showing electron tomography reconstruction of LipoCYS helicoids grown in the presence of CTAB (MP4)

Video S2 showing electron tomography reconstruction of LipoCYS helicoids grown in the presence of CTAC (MP4)

AUTHOR INFORMATION

Corresponding Authors

Ki Tae Nam – Department of Materials Science and Engineering, Seoul National University, Seoul 08826, Republic of Korea; orcid.org/0000-0001-6353-8877; Email: nkitae@snu.ac.kr

Sara Bals — EMAT and NANOLight Center of Excellence, University of Antwerp, Antwerp B-2020, Belgium;
ocid.org/0000-0002-4249-8017; Email: sara.bals@uantwerpen.be

Luis M. Liz-Marzán — CIC biomaGUNE, Basque Research and Technology Alliance (BRTA), Donostia-San Sebastián 20014, Spain; Ikerbasque, Bilbao 48009, Spain; Cinbio, University of Vigo, Vigo 36310, Spain; o orcid.org/0000-0002-6647-1353; Email: llizmarzan@cicbiomagune.es

Authors

In Han Ha – Department of Materials Science and Engineering, Seoul National University, Seoul 08826, Republic of Korea; orcid.org/0009-0005-8372-100X

- Kyle Van Gordon CIC biomaGUNE, Basque Research and Technology Alliance (BRTA), Donostia-San Sebastián 20014, Spain; orcid.org/0000-0003-3922-0951
- Robin Girod EMAT and NANOLight Center of Excellence, University of Antwerp, Antwerp B-2020, Belgium; orcid.org/0000-0001-7861-7818
- Jeong Hyun Han Department of Materials Science and Engineering, Seoul National University, Seoul 08826, Republic of Korea
- Evgenii Vlasov EMAT and NANOLight Center of Excellence, University of Antwerp, Antwerp B-2020, Belgium Sandra Baúlde CICA Centro Interdisciplinar de Química e Bioloxía, Facultade de Ciencias, Universidade da Coruña, A Coruña 15071, Spain; © orcid.org/0000-0002-7321-0039
- Jesús Mosquera CICA Centro Interdisciplinar de Química e Bioloxía, Facultade de Ciencias, Universidade da Coruña, A Coruña 15071, Spain; ⊙ orcid.org/0000-0001-6878-4567

Complete contact information is available at: https://pubs.acs.org/10.1021/acsnano.5c07744

Author Contributions

¶I.H.H., K.V.G., R.G., and J.H.H. contributed equally to this work. The manuscript was written through contributions of all authors. All authors have given approval to the final version of the manuscript

Notes

The authors declare no competing financial interest.

ACKNOWLEDGMENTS

The authors thank Prof. A. Criado for helpful discussions. This work was funded by the Spanish MCIN/AEI/10.13039/501100011033 (Grant PID2023-151281OB-I00 to L.M.L.-M, FPI Fellowship PRE2021-097588 to K.V.G., and Ramón y Cajal Fellowship RYC2019-027842-I to J.M.). S.B. and L.M.L.-M. acknowledge financial support from the European Research Council (ERC SYG 101166855, CHIRAL-PRO). R.G. acknowledges the support of a FWO fellowship under award 12A1 V25N. This research was supported by the Nano & Material Technology Development Program through the National Research Foundation of Korea (NRF) funded by Ministry of Science and ICT (RS-2024-00409405). K.T.N. appreciates the administrative and technical support from Institute of Engineering Research, Research Institute of Advanced Materials (RIAM), and SOFT foundry institute.

REFERENCES

- (1) Prodan, E.; Radloff, C.; Halas, N. J.; Nordlander, P. A Hybridization Model for the Plasmon Response of Complex Nanostructures. *Science* **2003**, 302, 419–422.
- (2) Fan, Z.; Govorov, A. O. Plasmonic Circular Dichroism of Chiral Metal Nanoparticle Assemblies. *Nano Lett.* **2010**, *10*, 2580–2587.
- (3) Goerlitzer, E. S. A.; Zapata-Herrera, M.; Ponomareva, E.; Feller, D.; Garcia-Etxarri, A.; Karg, M.; Aizpurua, J.; Vogel, N. Molecular-Induced Chirality Transfer to Plasmonic Lattice Modes. *ACS Photonics* **2023**, *10*, 1821–1831.
- (4) González-Rubio, G.; Kumar, V.; Llombart, P.; Díaz-Nunez, P.; Bladt, E.; Altantzis, T.; Bals, S.; Pena-Rodriguez, O.; Noya, E. G.; MacDowell, L. G.; et al. Disconnecting Symmetry Breaking from Seeded Growth for the Reproducible Synthesis of High Quality Gold Nanorods. *ACS Nano* **2019**, *13*, 4424–4435.
- (5) Liu, H.; Vladar, A. E.; Wang, P. P.; Ouyang, M. Tuning Geometric Chirality in Metallic and Hybrid Nanostructures by

- Controlled Nanoscale Crystal Symmetry Breaking. J. Am. Chem. Soc. 2023, 145, 7495–7503.
- (6) Ha, I. H.; Kim, R. M.; Han, J. H.; Im, S. W.; Jo, J.; Lee, Y. H.; Lv, J.; Lee, U. C.; Ahn, H. Y.; Lee, H. E.; et al. Synthesis of Chiral Ag, Pd, and Pt Helicoids inside Chiral Silica Mold. *J. Am. Chem. Soc.* **2024**, 146, 30741–30747.
- (7) Ni, B.; González-Rubio, G.; Van Gordon, K.; Bals, S.; Kotov, N. A.; Liz-Marzán, L. M. Seed-Mediated Growth and Advanced Characterization of Chiral Gold Nanorods. *Adv. Mater.* **2024**, *36*, No. e2412473.
- (8) Cho, N. H.; Kim, H.; Kim, J. W.; Lim, Y.-C.; Kim, R. M.; Lee, Y. H.; Nam, K. T. Chiral inorganic nanomaterials for biomedical applications. *Chem.* **2024**, *10*, 1052–1070.
- (9) Im, S. W.; Kim, R. M.; Han, J. H.; Ha, I. H.; Lee, H. E.; Ahn, H. Y.; Jo, E.; Nam, K. T. Synthesis of Chiral Gold Helicoid Nanoparticles Using Glutathione. *Nat. Protoc.* **2025**, *20*, 1082–1096.
- (10) Ni, B.; Mychinko, M.; Gomez-Grana, S.; Morales-Vidal, J.; Obelleiro-Liz, M.; Heyvaert, W.; Vila-Liarte, D.; Zhuo, X.; Albrecht, W.; Zheng, G.; et al. Chiral Seeded Growth of Gold Nanorods Into Fourfold Twisted Nanoparticles with Plasmonic Optical Activity. *Adv. Mater.* **2023**, 35, No. e2208299.
- (11) Im, S. W.; Zhang, D.; Han, J. H.; Kim, R. M.; Choi, C.; Kim, Y. M.; Nam, K. T. Investigating Chiral Morphogenesis of Gold Using Generative Cellular Automata. *Nat. Mater.* **2024**, *23*, 977–983.
- (12) Ito, T. H.; Salles, A. G.; Priebe, J. P.; Miranda, P. C.; Morgon, N. H.; Danino, D.; Mancini, G.; Sabadini, E. Generation of a Chiral Giant Micelle. *Langmuir* **2016**, *32*, 8461–8466.
- (13) González-Rubio, G.; Mosquera, J.; Kumar, V.; Pedrazo-Tardajos, A.; Llombart, P.; Solís, D. M.; Lobato, I.; Noya, E. G.; Guerrero-Martínez, A.; Taboada, J. M.; et al. Micelle-directed chiral seeded growth on anisotropic gold nanocrystals. *Science* **2020**, *368*, 1472–1477.
- (14) Heyvaert, W.; Pedrazo-Tardajos, A.; Kadu, A.; Claes, N.; González-Rubio, G.; Liz-Marzán, L. M.; Albrecht, W.; Bals, S. Quantification of the Helical Morphology of Chiral Gold Nanorods. *ACS Materials Lett.* **2022**, *4*, 642–649.
- (15) Vlasov, E.; Heyvaert, W.; Ni, B.; Van Gordon, K.; Girod, R.; Verbeeck, J.; Liz-Marzan, L. M.; Bals, S. High-Throughput Morphological Chirality Quantification of Twisted and Wrinkled Gold Nanorods. *ACS Nano* **2024**, *18*, 12010–12019.
- (16) Van Gordon, K.; Ni, B.; Girod, R.; Mychinko, M.; Bevilacqua, F.; Bals, S.; Liz-Marzán, L. M. Single Crystal and Pentatwinned Gold Nanorods Result in Chiral Nanocrystals with Reverse Handedness. *Angew. Chem., Int. Ed.* **2024**, *63*, No. e202403116.
- (17) Xu, L.; Wang, X.; Wang, W.; Sun, M.; Choi, W. J.; Kim, J. Y.; Hao, C.; Li, S.; Qu, A.; Lu, M.; et al. Enantiomer-Dependent Immunological Response to Chiral Nanoparticles. *Nature* **2022**, *601*, 366–373.
- (18) Cho, N. H.; Byun, G. H.; Lim, Y. C.; Im, S. W.; Kim, H.; Lee, H. E.; Ahn, H. Y.; Nam, K. T. Uniform Chiral Gap Synthesis for High Dissymmetry Factor in Single Plasmonic Gold Nanoparticle. *ACS Nano* **2020**, *14*, 3595–3602.
- (19) Van Gordon, K.; Baulde, S.; Mychinko, M.; Heyvaert, W.; Obelleiro-Liz, M.; Criado, A.; Bals, S.; Liz-Marzán, L. M.; Mosquera, J. Tuning the Growth of Chiral Gold Nanoparticles Through Rational Design of a Chiral Molecular Inducer. *Nano Lett.* **2023**, 23, 9880–9886.
- (20) Van Gordon, K.; Girod, R.; Bevilacqua, F.; Bals, S.; Liz-Marzán, L. M. Structural and Optical Characterization of Reaction Intermediates during Fast Chiral Nanoparticle Growth. *Nano Lett.* **2025**, 25, 2887–2893.
- (21) Obelleiro-Liz, M.; Martín, V. F.; Solís, D. M.; Taboada, J. M.; Obelleiro, F.; Liz-Marzán, L. M. Influence of Geometrical Parameters on the Optical Activity of Chiral Gold Nanorods. *Adv. Optical Mater.* **2023**, *11*, 2203090.
- (22) Zhuo, X.; Mychinko, M.; Heyvaert, W.; Larios, D.; Obelleiro-Liz, M.; Taboada, J. M.; Bals, S.; Liz-Marzán, L. M. Morphological and Optical Transitions during Micelle-Seeded Chiral Growth on Gold Nanorods. *ACS Nano* **2022**, *16*, 19281–19292.

- (23) Namgung, S. D.; Kim, R. M.; Lim, Y. C.; Lee, J. W.; Cho, N. H.; Kim, H.; Huh, J. S.; Rhee, H.; Nah, S.; Song, M. K.; et al. Circularly Polarized Light-Sensitive, Hot Electron Transistor with Chiral Plasmonic Nanoparticles. *Nat. Commun.* **2022**, *13*, 5081.
- (24) Girod, R.; Vlasov, E.; Liz-Marzán, L. M.; Bals, S. Three-Dimensional Electron Microscopy of Chiral Nanoparticles: From Imaging to Measuring. *Nano Lett.* **2025**, *25*, 7629–7640.
- (25) Vlasov, E.; Skorikov, A.; Sánchez-Iglesias, A.; Liz-Marzán, L. M.; Verbeeck, J.; Bals, S. Secondary Electron Induced Current in Scanning Transmission Electron Microscopy: An Alternative Way to Visualize the Morphology of Nanoparticles. *ACS Materials Lett.* **2023**, *5*, 1916–1921.
- (26) Ahn, H.-Y.; Lee, H.-E.; Jin, K.; Nam, K. T. Extended Gold Nano-Morphology Diagram: Synthesis of Rhombic Dodecahedra Using CTAB and Ascorbic Acid. *J. Mater. Chem. C* **2013**, *1*, 6861–6868
- (27) Lee, H. E.; Ahn, H. Y.; Mun, J.; Lee, Y. Y.; Kim, M.; Cho, N. H.; Chang, K.; Kim, W. S.; Rho, J.; Nam, K. T. Amino-Acid- and Peptide-Directed Synthesis of Chiral Plasmonic Gold Nanoparticles. *Nature* **2018**, *556*, 360–365.
- (28) Lee, H. E.; Kim, R. M.; Ahn, H. Y.; Lee, Y. Y.; Byun, G. H.; Im, S. W.; Mun, J.; Rho, J.; Nam, K. T. Cysteine-Encoded Chirality Evolution in Plasmonic Rhombic Dodecahedral Gold Nanoparticles. *Nat. Commun.* **2020**, *11*, 263.
- (29) Zheng, J.; Boukouvala, C.; Lewis, G. R.; Ma, Y.; Chen, Y.; Ringe, E.; Shao, L.; Huang, Z.; Wang, J. Halide-Assisted Differential Growth of Chiral Nanoparticles with Threefold Rotational Symmetry. *Nat. Commun.* **2023**, *14*, 3783.
- (30) Wu, F.; Li, F.; Tian, Y.; Lv, X.; Luan, X.; Xu, G.; Niu, W. Surface Topographical Engineering of Chiral Au Nanocrystals with Chiral Hot Spots for Plasmon-Enhanced Chiral Discrimination. *Nano Lett.* **2023**, 23, 8233–8240.
- (31) Almora-Barrios, N.; Novell-Leruth, G.; Whiting, P.; Liz-Marzán, L. M.; López, N. Theoretical Description of the Role of Halides, Silver, and Surfactants on the Structure of Gold Nanorods. *Nano Lett.* **2014**, *14*, 871–875.
- (32) Song, T.; Gao, F.; Guo, S.; Zhang, Y.; Li, S.; You, H.; Du, Y. A Review of the Role and Mechanism of Surfactants in the Morphology Control of Metal Nanoparticles. *Nanoscale* **2021**, *13*, 3895–3910.
- (33) Scarabelli, L.; Sánchez-Iglesias, A.; Perez-Juste, J.; Liz-Marzán, L. M. A "Tips and Tricks" Practical Guide to the Synthesis of Gold Nanorods. *J. Phys. Chem. Lett.* **2015**, *6*, 4270–4279.
- (34) Lohse, S. E.; Burrows, N. D.; Scarabelli, L.; Liz-Marzán, L. M.; Murphy, C. J. Anisotropic Noble Metal Nanocrystal Growth: The Role of Halides. *Chem. Mater.* **2014**, *26*, 34–43.
- (35) Buda, A. B.; Mislow, K. A Hausdorff chirality measure. *J. Am. Chem. Soc.* **1992**, *114*, 6006–6012.
- (36) Kim, J.-Y.; Yeom, J.; Zhao, G.; Calcaterra, H.; Munn, J.; Zhang, P.; Kotov, N. Assembly of Gold Nanoparticles into Chiral Superstructures Driven by Circularly Polarized Light. *J. Am. Chem. Soc.* **2019**, *141*, 11739–11744.
- (37) Han, J. H.; Lim, Y. C.; Kim, R. M.; Lv, J.; Cho, N. H.; Kim, H.; Namgung, S. D.; Im, S. W.; Nam, K. T. Neural-Network-Enabled Design of a Chiral Plasmonic Nanodimer for Target-Specific Chirality Sensing. *ACS Nano* **2023**, *17*, 2306–2317.
- (38) Googasian, J. S.; Lewis, G. R.; Woessner, Z. J.; Ringe, E.; Skrabalak, S. E. Seed-Directed Synthesis of Chiroptically Active Au Nanocrystals of Varied Symmetries. *Chem. Commun.* **2022**, *58*, 11575–11578.
- (39) Googasian, J. S.; Skrabalak, S. E. Practical Considerations for Simulating the Plasmonic Properties of Metal Nanoparticles. *ACS Phys. Chem. Au.* **2023**, *3*, 252–262.
- (40) Han, J. H.; Ha, I. H.; Cha, J. H.; Jo, J.; Lv, J.; Im, S. W.; Cho, S. H.; Lim, D.; Kim, R. M.; Kim, M.; et al. Isotropic Size Control of Chiral Gold Helicoids. *J. Phys. Chem. C* **2025**, *129*, 7020–7030.
- (41) Hu, L.; Huang, Y.; Pan, L.; Fang, Y. Analyzing Intrinsic Plasmonic Chirality by Tracking the Interplay of Electric and Magnetic Dipole Modes. *Sci. Rep.* **2017**, *7*, No. 11151.

- (42) Vora, H. D.; Johnson, M.; Brea, R. J.; Rudd, A. K.; Devaraj, N. K. Inhibition of NRAS Signaling in Melanoma through Direct Depalmitoylation Using Amphiphilic Nucleophiles. *ACS Chem. Biol.* **2020**, *15*, 2079–2086.
- (43) Wu, H.-L.; Tsai, H.-R.; Hung, Y.-T.; Lao, K.-U.; Liao, C.-W.; Chung, P.-J.; Huang, J.-S.; Chen, I.-C.; Huang, M. H. A Comparative Study of Gold Nanocubes, Octahedra, and Rhombic Dodecahedra as Highly Sensitive SERS Substrates. *Inorg. Chem.* **2011**, *50*, 8106–8111.
- (44) Li, C.; Tardajos, A. P.; Wang, D.; Choukroun, D.; Van Daele, K.; Breugelmans, T.; Bals, S. A Simple Method to Clean Ligand Contamination on TEM Grids. *Ultramicroscopy* **2021**, 221, No. 113195.
- (45) Vanrompay, H.; Skorikov, A.; Bladt, E.; Béché, A.; Freitag, B.; Verbeeck, J.; Bals, S. Fast versus Conventional HAADF-STEM Tomography of Nanoparticles: Advantages and Challenges. *Ultramicroscopy* **2021**, 221, No. 113191.
- (46) van Aarle, W.; Palenstijn, W. J.; De Beenhouwer, J.; Altantzis, T.; Bals, S.; Batenburg, K. J.; Sijbers, J. The ASTRA Toolbox: A Platform for Advanced Algorithm Development in Electron Tomography. *Ultramicroscopy* **2015**, *157*, 35–47.
- (47) van Aarle, W.; Palenstijn, W. J.; Cant, J.; Janssens, E.; Bleichrodt, F.; Dabravolski, A.; De Beenhouwer, J.; Joost Batenburg, K.; Sijbers, J. Fast and Flexible X-Ray Tomography Using the ASTRA Toolbox. *Opt. Express* **2016**, *24*, 25129–25147.
- (48) Buda, A. B.; Mislow, K. A Hausdorff Chirality Measure. J. Am. Chem. Soc. 1992, 114, 6006–6012.
- (49) Kim, J.-Y.; Yeom, J.; Zhao, G.; Calcaterra, H.; Munn, J.; Zhang, P.; Kotov, N. Assembly of Gold Nanoparticles into Chiral Superstructures Driven by Circularly Polarized Light. *J. Am. Chem. Soc.* **2019**, *141*, 11739–11744.
- (50) Gao, F.; Han, L. Implementing the Nelder-Mead Simplex Algorithm with Adaptive Parameters. *Comput. Optim. Appl.* **2012**, *51*, 259–277.
- (51) Otsu, N. A. Threshold Selection Method from Gray-Level Histograms. *IEEE Trans. Syst. Man. Cybern.* **1979**, *9*, 62–66.
- (52) Bradley, D.; Roth, G. Adaptive Thresholding Using the Integral Image. *J. Graphics Tools* **2007**, *12*, 13–21.

